Three-dimensional Fluid-Structure Interaction Diagnostics Using a Single Camera

Bibek Sapkota[a], Holger Mettelsiefen[a], Vrishank Raghav[a,*] and Brian S. Thurow[a,*]

[a]Department of Aerospace Engineering, Auburn University, Auburn, AL, 36849, USA

ARTICLE INFO

Keywords:
Flexible membrane
structural motion
3D flow field
light field camera
Proper orthogonal decomposition

ABSTRACT

A new method for fluid-structure interaction (FSI) diagnostics to simultaneously capture time-resolved three-dimensional, three-component (3D3C) velocity fields and structural deformations using a single light field camera is presented. A light field camera encodes both spatial and angular information of light rays collected by a conventional imaging lens that allows for the 3D reconstruction of a scene from a single image. Building upon this capability, a light field fluid-structure interaction (LF FSI) methodology is developed with a focus on experimental scenarios with low optical access. Proper orthogonal decomposition (POD) is used to separate particle and surface information contained in the same image. A correlation-based depth estimation technique is introduced to reconstruct instantaneous surface positions from the disparity between angular perspectives and conventional particle image velocimetry (PIV) is used for flow field reconstruction. Validation of the methodology is achieved using synthetic images of simultaneously moving flat plates and a vortex ring with a small increase in uncertainty under ~ 0.5 microlenses observed in both flow and structure measurement compared to independent measurements. The method is experimentally verified using a flat plate translating along the camera's optical axis in a flow field with varying particle concentrations. Finally, simultaneous reconstructions of the flow field and surface shape around a flexible membrane are presented, with the surface reconstruction further validated using simultaneously captured stereo images. The findings indicate that the LF FSI methodology provides a new capability to simultaneously measure large-scale flow characteristics and structural deformations using a single camera.

1. Introduction

The interplay between fluid dynamics and structural mechanics gives rise to a cascade of effects, where changes in flow motion and surface deformation become intricately linked at the interface of the fluid and the structure. The relationship between fluid and structure is reciprocal: structural motion alters the boundary conditions at the fluid interface, causing fluctuations in pressure and/or viscous forces, and the interaction at the fluid-structure interface can lead to changes in structural motion. Thus, fluid-structure interaction (FSI) is a multiphysics interaction that is integral to understanding many applications including biomechanics, turbomachinery, aeroelastic coupling, sedimentation, hydro-elasticity, etc. (Sigrist, 2015).

Due to the prevalence of FSI (Hou et al., 2012), considerable effort has been focused on quantifying and understanding the underlying physics. However, a challenge for both experiments and computations is that the fluid-structure interface in cases such as flexible membranes can be subject to large deformations (Griffith and Patankar, 2020). Flexible membranes in steady flow have been investigated in several canonical configurations, including conventional flags (Argentina and Mahadevan, 2005), bending membranes (Vogel, 1989), and inverted flags (Dou et al., 2020), among others. Here, the flexible membrane exhibits flow-induced flutter (high-frequency structural oscillations) where the Reynolds number (Re), non-dimensional rigidity (β), mass ratio (μ), and aspect ratio (AR) as defined in Eq. 1, are important governing dimensionless parameters (Shelley and Zhang, 2011). These studies have investigated fundamental FSI physics, including effects of added mass, vortex shedding, drag-induced tension, among others, to map unstable and stable regimes and the associated transitions. Furthermore, these studies have elucidated inherent aspects such as bi-stability of flutter modes (Zhang et al., 2000) and hysteresis in the damping of flutter (Watanabe et al., 2002).

*Corresponding authors
raghav@auburn.edu (V. Raghav); thurow@auburn.edu (B.S. Thurow)
ORCID(s): 0000-0001-8667-4409 (V. Raghav); 0000-0002-2166-9067 (B.S. Thurow)

$$Re = \frac{UL}{\nu} \qquad \beta = \frac{B}{\rho_f U^2 L^3} \qquad \mu = \frac{\rho_m t_m}{\rho_f L} \qquad AR = \frac{W}{L} \tag{1}$$

where the working fluid properties are defined by ν the kinematic viscosity, ρ_f the density, and U the bulk average velocity. The properties of the homogeneous and isotropic flexible membrane are defined by L the length, W the width, ρ_m the density, t_m the thickness, and B the flexural rigidity.

For most FSI problems, analytical solutions to the physically coupled equations are challenging to obtain, and while experimental methods are improving, they are still limited in scope. Therefore, the predominant choice to investigate FSI physics has been numerical simulations with good progress over the last few decades starting from loosely coupled 2D FSI methods to tightly coupled 3D simulations (Sotiropoulos and Borazjani, 2009). On the other hand, experimental methods have primarily focused on lower-fidelity decoupled approaches with flow field measurements obtained separately from one- or two-dimensional structural motion (Kalmbach and Breuer, 2013; Nila et al., 2016). Digital image correlation (DIC) and particle image velocimetry (PIV) have emerged as popular optical diagnostic techniques for structure and flow measurement, respectively, because of their non-intrusive nature and high spatial resolution. The current state-of-the-art FSI diagnostic method involves the use of multiple cameras to perform DIC and PIV simultaneously. Multi-camera based simultaneous 2D-2C/3C PIV and 2D/3D DIC measurements have been conducted by Giovannetti et al. (2017) on flexible aerofoils under fluid loading, Bleischwitz et al. (2017) on rigid flat plates and flexible membrane wings flying in ground effect conditions, Zhang and Porfiri (2019) to evaluate the structural response and hydrodynamic loading in water-backed impact, D'Aguanno et al. (2023) to analyze the panel flutter induced by an impinging shock-wave, and Bhargav et al. (2024) to study the relationship between tube geometry and flow field of a collapsible tube etc. Recent advances have led to simultaneous 3D time-resolved measurements of both the flow field and structural motion using extensive six-camera setups (Safi et al., 2017) or similar (Zhang et al., 2020), which are expensive and in some cases infeasible due to limited optical access (due to size/scale of the flow facility). Particularly in biomedical, combustion, or super- or hypersonic applications, restricted optical access places fundamental limits on existing diagnostics and necessitates a new approach to accurately and simultaneously measure time-resolved 3D flow fields and structural motion. To this end, this work leverages recent advances in light field imaging and plenoptic cameras to establish a new approach for FSI diagnostics.

In conventional cameras, the entire lens aperture focuses light rays onto a point on the image sensor. In contrast, a plenoptic camera (a type of light field camera) incorporates a dense microlens array (MLA) positioned close to the sensor plane, redirecting light rays from different sections of the aperture to specific pixels on the sensor plane (Ng et al., 2005; Adelson and Wang, 1992). This unique arrangement enables a plenoptic image to capture 4D light field information, including both positional and directional characteristics. By sampling a pixel (u, v) from each subimage (s, t) formed by the microlens, a plenoptic image can generate multiple (~ 100) perspective views over a small baseline. These perspectives have a higher depth of field than conventional camera images because they are sampled from small-aperture subimages. This capability has been used to develop single-camera-based 3D flow measurement techniques like plenoptic PIV (Skupsch and Brücker, 2013; Fahringer et al., 2015), plenoptic particle tracking velocimetry (PTV) (Liu et al., 2019; Moaven et al., 2024) and plenoptic background oriented schlieren (BOS) (Klemkowsky et al., 2017). In this work, we use the 3D imaging capability of a plenoptic camera to formulate a novel methodology for fluid-structure interaction diagnostics.

Capturing both flow field and structural motion information in the same image poses a challenge as the signals must be separated before conventional analysis methods can be applied. Mitrotta et al. (2022) and Saiz et al. (2022) used distinct surface markers to identify and separate surface information from combined information in a multi-camera system. This makes the resolution of surface points and the quality of the flow field dependent on the size and number of marker points. Song et al. (2022) used the visual hull method and the binocular stereo vision method to identify surface bubbles in a particle field. Giovannetti et al. (2017) used green and magenta filters in separate PIV and DIC cameras with illumination from the corresponding wavelength. However, these approaches are generally not feasible with a single-camera setup. Our approach uses speckle pattern images and a data-driven method to separate flow and structure signals. Correlation-based depth estimation enables marker-independent, high-resolution surface reconstruction.

In this work, we develop and test a correlation-based surface reconstruction technique using a plenoptic camera. We apply a POD-based decomposition approach to separate flow and structure signals from combined images. Building on

these approaches, we formulate, test, and assess the light field fluid-structure interaction (LF FSI) methodology, with validation focused on the accuracy of structure reconstruction in the presence of particles. The detailed framework of our methodology is introduced in Section 2. Section 3 explains the POD-based separation of particle and structure images. Section 4 covers the steps of the novel plenoptic surface reconstruction technique. The synthetic analysis performed to validate the surface reconstruction technique, the POD-based separation, and the overall LF FSI methodology are presented in Section 5. Test experiments to validate the methodology under multiple flow conditions are presented in Section 6. Finally, the observations and conclusions of our work are presented in Section 7.

2. Overview of LF FSI methodology

The proposed methodology is summarized in Figure 1 with each of the individual steps described below.

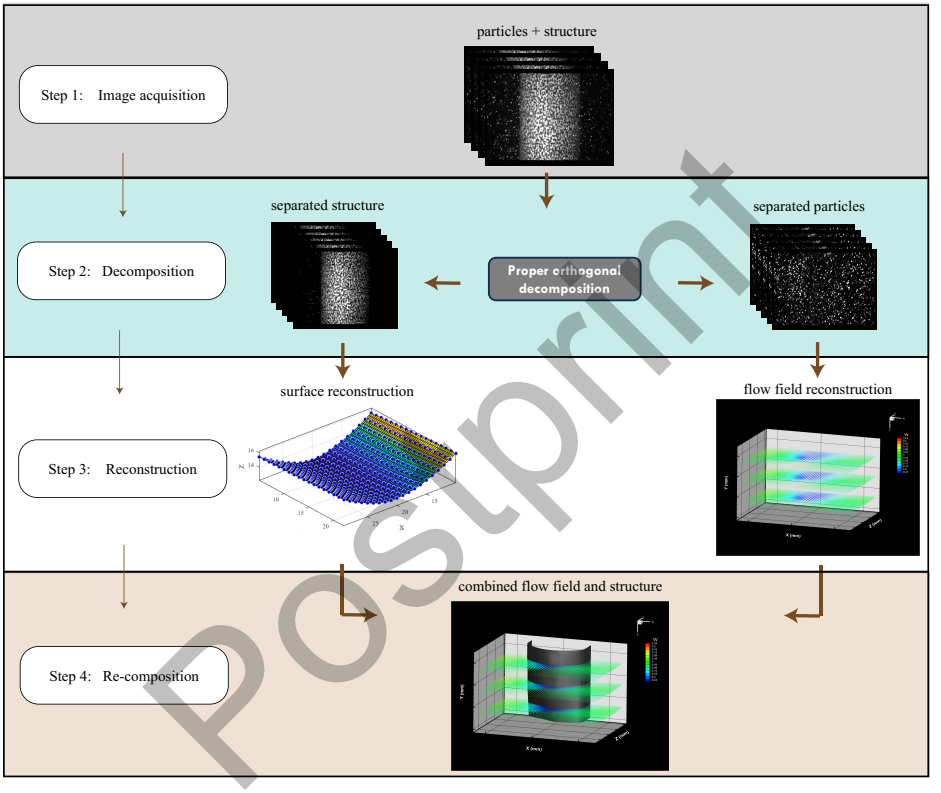

Figure 1: Schematic workflow of LF FSI diagnostics methodology.

1. *Image acquisition:* First, fluid and structure information are captured simultaneously in a single image using a plenoptic camera. The flow field information is embedded in neutrally buoyant tracer particles that travel with the flow while the structure's surface is coated with a speckle pattern for correlation-based depth estimation. The intensities of both the particle images and the surface speckle pattern are designed to fall within the dynamic range of the camera. Time-resolved images capture flow and surface data, although this method is equally applicable to frame-straddled imaging.
2. *Decomposition:* Second, the flow field and structural signals are separated using proper orthogonal decomposition (POD), following assumptions similar to Mendez et al. (2017) for background removal in PIV. We assume that the contribution of particle information is spatially random such that its energy is uniformly distributed across all POD modes. It is also assumed that the correlation between surface and particle information is minimal and the information of the surface is captured within a few high-energy eigenmodes. This is valid as long as the spatial description of the structure is statistically correlated over time in contrast to randomly distributed particles. The details of the application of POD-based decomposition are given in Section 3.

3. *Reconstruction:* Third, the 3D flow field and surface are reconstructed from separated images of particles and speckle patterns. The 3D flow field is determined using methods already established for plenoptic PIV. Surface reconstruction is carried out in a novel fashion by relating the depth to the disparity obtained from different angular perspectives where a correlation-based technique is used to determine the disparity. Details and benchmarking of plenoptic surface reconstruction are provided in Section 4.
4. *Re-composition:* After both flow and surface data are determined, they are recombined to study the motion of both fluid and structure together. Since both the fluid and the structure measurement domain are the same and obtained from a common calibration, a direct re-composition of the fluid and structure motion can be obtained and used to study FSI physics.

Our FSI methodology also applies to conventional multi-camera experiments but is specifically designed for plenoptic imaging, and thus termed light field fluid-structure interaction (LF FSI). Specifically, the POD-based particle/surface separation is equally applicable with conventional camera images; however, surface reconstruction with the direct cross-correlation technique is not optimal for conventional multi-camera experiments as the disparity between images will be relatively large compared to images obtained with a plenoptic camera. Feature matching-based multi-camera surface reconstruction can be a possible alternative in such scenarios. The flow measurement techniques are also similar for both conventional and plenoptic imaging albeit with different levels of performance depending on the camera configuration with plenoptic PIV characterized by larger degrees of uncertainty in the depth direction.

3. Decomposition into particle and surface images

Proper orthogonal decomposition (POD) is a well-established technique used to extract coherent structures from data by transforming correlated variables into a set of orthonormal basis functions that optimally represent the dataset. It has been widely applied in video analysis and noise reduction in image sequences, including PIV images, where it helps separate dominant background structures from transient particles (Mendez et al., 2017; Baghaie, 2019). Our work employs POD for separating particles and background, similar to Mendez et al. (2017), in the context of plenoptic imaging of fluid-structure interaction. In this process, the image sequence is reshaped into a single matrix, with each image represented as a column vector. The reduced-order approximation of this matrix is obtained using a truncated singular value decomposition (SVD), ensuring minimal loss in the least-squares sense. By leveraging the differences in temporal coherence between surface structures and particle motion, the surface is extracted using dominant eigenmodes, while the particle information is reconstructed from the remaining low-rank modes.

Our separation methodology assumes that the surface information is captured by a few dominant eigenmodes, while the moving particle information is evenly distributed among a significantly larger number of low-rank eigenmodes, meaning the dominant eigenmodes carry minimal particle information. If either condition is not met, a distinct separation of particle and surface images using POD is not possible. Examples of such cases include scenarios where structural motion is highly random, such that the energy of coherent structure capturing the structural motion is evenly distributed over many eigenmodes. Similar scenarios also occur when the particles and structure move together over longer periods of time or particles and structure both are stationary. Factors such as the number of images available for decomposition and the number of cycles of structure motion captured also affect the quality of separation. Since these factors vary with the nature of the experiment and the complexity and variability of surface motion, a detailed quantification of such scenarios is difficult and beyond the scope of this work. In this study, utilizing multiple cycles ($\sim$ 10 cycles) of structural movements and employing over 1000 images for POD has given us a distinct separation.

4. Structural motion and flow field reconstruction

4.1. Stereovision and plenoptic surface reconstruction

Stereovision is a method for estimating depth based on either the apparent motion of a camera or the disparity between two cameras. The disparity is related to the depth through Equation 2 (Roberts and Thurow, 2017).

$$\frac{1}{S_0} = \frac{1}{F} - \frac{1}{S_{if}}\left(1 - \frac{d}{B}\right) \tag{2}$$

This relation is formulated from a thin lens equation and similar triangle relations. Figure 2 shows a schematic to visualize this relationship for a plenoptic camera. Here, S_0 is the object distance, F is the focal length of the main lens,

d is the disparity between two perspectives, S_{if} is the separation between the main lens and the microlens array, and B is the baseline between two perspectives. The baseline can be calculated using Equation 3 where f is the focal length of the microlens and h is the absolute value of (u, v) on the sensor.

$$B = -\frac{S_{if} \times h}{f} \tag{3}$$

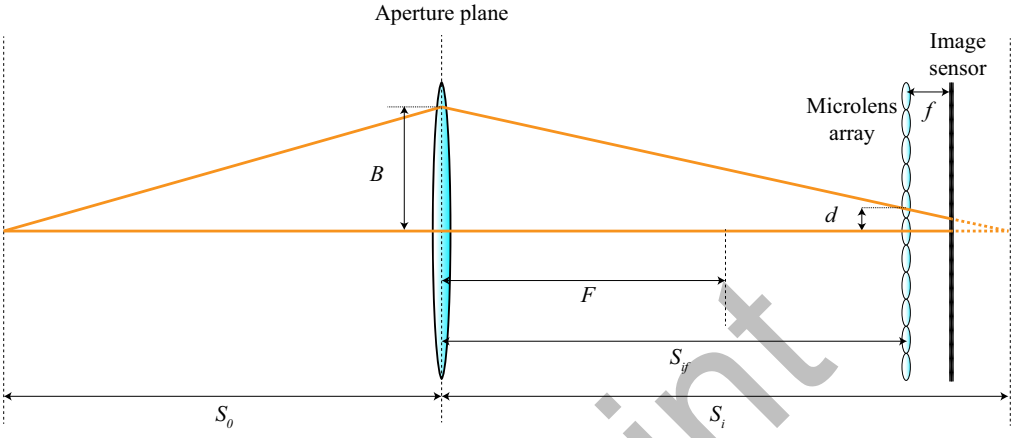

Figure 2: Optical arrangement showing disparity (d) and aperture displacement (B).

In a plenoptic camera, cross-correlation can be calculated between any two arbitrary perspectives. The uniqueness of plenoptic-DIC lies in the abundance of available perspectives, enabling the potential measurement of numerous disparities for a single point in object space. In this work, we leverage this information to develop a robust methodology for surface reconstruction. This is meant to improve the accuracy of surface measurement in the presence of occlusions or noise, such as that produced by the residual signal from seed particles that may be present in simultaneous PIV/DIC measurements.

4.1.1. Disparity bundling

In this section, we introduce a correlation-based surface reconstruction technique for a plenoptic camera that is referred to as disparity bundling. Figure 3 shows the individual steps. This methodology is inspired by the cross-correlation-based depth estimation technique (Roberts and Thurow, 2017) and the light field ray bundle technique (Clifford et al., 2019) for plenoptic cameras. Here, perspective images (~ 100) are generated from a single image by sampling the same relative pixel (u, v) from each subimage (s, t). A reference image is defined among all available perspectives and all other perspectives are considered displaced images compared to the reference image. In this work, we use the center perspective (*i.e.* $u = 0,\ v = 0$) as a reference image for convenience.

Next, cross-correlation is performed between the reference image and all other perspectives using the window-based multigrid iterative method (Scarano and Riethmuller, 2000), with the normalized correlation map weighted by a Blackman window. Subpixel accuracy is achieved via 2D Gaussian fitting around the peak, identifying disparities between the reference and other perspectives. Before further using this disparity, we use the acquired strength of correlation between two perspectives to identify outlier disparity values. The signal-to-noise ratio is defined as the ratio of the highest to the second-highest peak on the map. A disparity with high confidence (SNR > 4) is generally considered optimal but this threshold can be adjusted based on data quality. The SNR could also be defined on the basis of the strength of the correlation itself. However, an optimum threshold value may be unique for each new experiment.

Then, the obtained disparities are consolidated for each window. When the disparities of the point (s, t) in the reference image are gathered from all the correlation maps, this yields the updated position of this window in all other perspectives. Consequently, all pairs of s and t are aggregated for all combinations of u and v. It is noted that the bundling step in this methodology is simpler compared to the bundling process based on the minimum distance between rays, as discussed in Clifford et al. (2019).

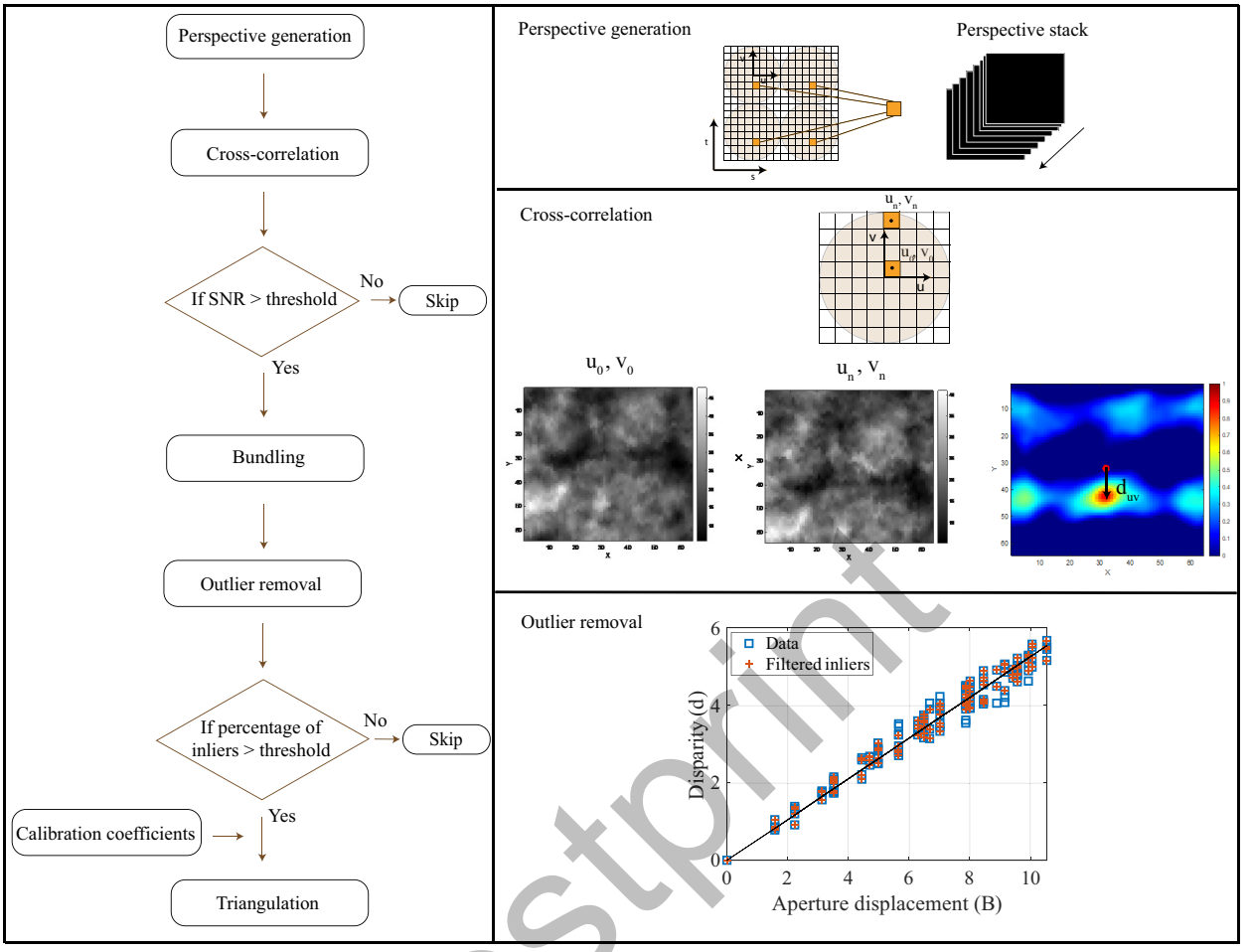

Figure 3: Steps of disparity bundling methodology for surface reconstruction.

The acquired disparity is then further filtered to retain high-confidence disparity values for triangulation. Occlusions, such as PIV particles not fully removed by POD decomposition, can cause erroneous disparities. With a multitude of available disparity values from various perspectives, low-confidence values are excluded to ensure robust depth estimation. Identifying these outliers involves leveraging prior knowledge of the linear relationship between disparity and aperture displacement. As detailed in Roberts and Thurow (2017), a line is fit through the acquired disparity and aperture displacement values. Subsequently, the Random Sample Consensus (RANSAC) algorithm is used to determine the best-fit slope, ensuring that the y-intercept is zero, as the disparity of an image with itself is zero. Disparities deviating by more than 0.2 microlenses are classified as outliers. Subsequently, the filtered data are accepted, and the bundle is updated. A final check is performed by calculating the percentage of inlier disparity compared to the total available disparities. If the value is greater than the set threshold, the inlier data proceed to the next step.

Finally, the depth location is determined by triangulating inlier image points using inverted Direct Light Field Calibration (DLFC) (Clifford et al., 2019). DLFC (Hall et al., 2018) is a polynomial-based mapping of object space points (x, y, z) to image space $[s, t] = P(x, y, z, u, v)$. The updated bundle comprises a list of points in the image space (s, t, u, v), and the desired variables are the points in the 3D space (x, y, z). This is done using a non-linear least-squares optimization with MATLAB's `lsqnonlin` function (Moré, 2006), yielding a point cloud of surface points in object space.

4.2. Flow field reconstruction

Flow field reconstruction is performed by applying the plenoptic particle image velocimetry (PPIV) technique to the particle images. PPIV comprises two steps, 3D particle volume reconstruction and cross-correlation. In particle volume

reconstruction, perspective image intensities are projected onto the discretized volume space and subsequently refined using the multiplicative algebraic reconstruction technique (MART) (Elsinga et al., 2006). MART is a variation of the algebraic reconstruction technique that iteratively updates the intensity of particles based on the ratio of reprojected image intensity to the summation of intensity along the line of sight. Cross-correlation is performed to determine the displacement of particles from two consecutive volumes. It is based on an iterative multi-grid window deformation technique as described in Scarano and Riethmuller (2000). Interested readers are directed to Fahringer et al. (2015) for further details on the implementation of this technique in the context of plenoptic PIV.

5. Evaluation of the methodology using synthetic data

5.1. Assessment of plenoptic surface reconstruction

To analyze the performance of the plenoptic surface reconstruction technique, a synthetic analysis is performed where a flat surface is simulated within the measurement domain, placed within -20 mm (closer to the camera) to 20 mm (farther) around the focal plane. This notation of location relative to the measurement volume is maintained throughout the paper. The surface is marked by randomly placed round dots forming a speckle pattern. Light rays originating from the random dots are propagated to the plenoptic camera using ray tracing equations and ray transfer matrix models of the medium, main lens, and microlenses, reaching the image sensor at a prescribed distance that maintains a magnification of -0.5. The size of these dots is around 5 to 9 pixels, ensuring that they are larger than normal PIV particles in image space. The process of generating synthetic speckle pattern images is similar to generating synthetic particle images and the readers are referred to Fahringer et al. (2015) for further details. The use of these random dots as speckle pattern is observed to provide a good correlation map for disparity measurement. The details of the configuration used for the synthetic analysis are tabulated in Table 1.

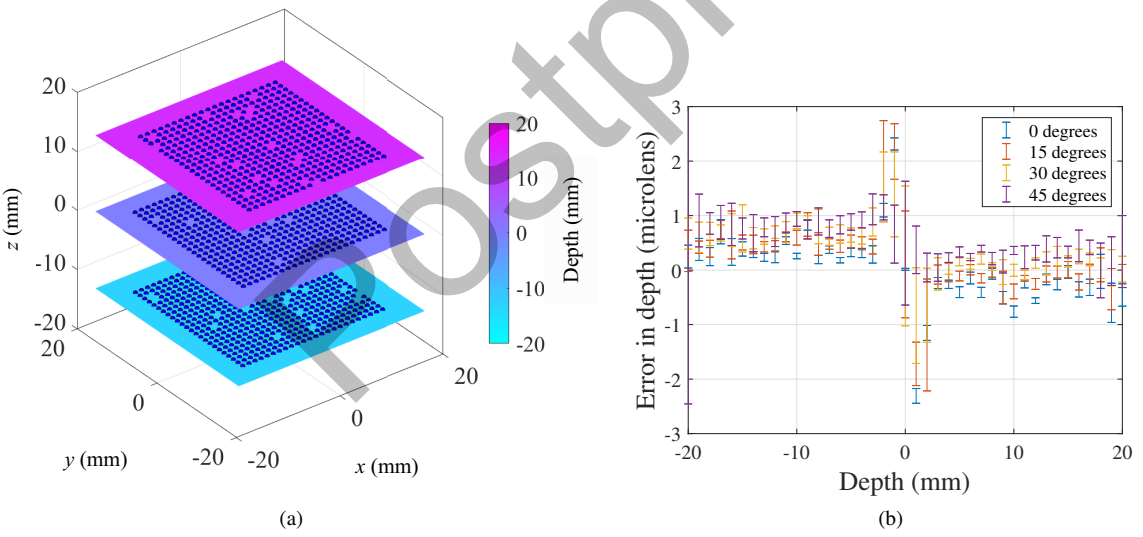

Figure 4: (a) Synthetic surface reconstruction at different depth locations. The blue dots represent the reconstructed points derived from the disparity map. Some missing points are low confidence that did not exceed the threshold limits for reconstruction and were removed at various stages. (b) Distribution of depth-wise error in surface reconstruction when the surface is positioned at different angles.

Figure 4.a shows the reconstruction of a synthetic surface with a point cloud at different depth locations using the disparity bundling method. A surface is fitted on the point cloud using the `fit` function in MATLAB. The color bar indicates the reconstructed depth location of the surface. The reconstructed surface is approximately flat as the standard deviation in the position of the reconstructed point cloud is only around 0.12 microlenses (0.02 mm). This illustrates that the disparity bundling method reconstructs the surface with precision within a fraction of a microlens from a single plenoptic image.

Table 1
Configuration of synthetic analysis for surface reconstruction

Equipment	**Setup**
Camera	Imperx B6620 CCD camera Pixel size: 0.0055 mm Resolution: 6600 × 4400
Micro-lens	Focal length: 0.308 mm Radius: 0.077 mm
Main lens	85 mm
Surface reconstruction	**Configuration**
Magnification	-0.5
Speckle pattern	5-9 microlenses
Volume of interest	x=[-20 to 20] mm, y=[-20 to 20] mm, z=[-20 to 20] mm
Perspective image size	942 × 628
Number of perspectives	81
Correlation window size	[64,32,32]
Window overlap	[32,16,16]
RANSAC outlier threshold	0.2 microlenses

To further assess the performance of surface reconstruction at different angles from the camera view, the synthetic surface is positioned at angles of 0, 15, 30, and 45 degrees. Since the uncertainty in depth estimation varies along the depth, the plate is positioned at different depth locations within the volume. The standard deviation of the error of estimated depth for the four angles is 0.123, 0.238, 0.270 and 0.347 microlenses, respectively. Figure 4.b shows the distribution of errors in the depth measurement at different depth locations for different plate angles. The uncertainty is low for the plate angle of 0 degrees compared to other angles. Additionally, there is a large bias in error around the focal plane at 0 mm for this angle. This is because the disparity close to the focal plane is very small due to low angular information. This is a well-known limitation of plenoptic cameras (Roberts and Thurow, 2017). The sharpness of the image is also higher towards the focal plane. This causes the correlation and hence the reconstructed surface position to bias toward the focal plane. For an inclined plate, the uncertainty is high close to the focal plane because the plate covers both sides of the focal plane, leading to higher uncertainty related to biases on both sides of the depth. In addition, we also observe a small bias in overall error distribution as the plate angle increases. Overall, based on results from the depth-wise error graph, we can infer that the surface positioned away from the focal plane but within the limits of the depth of field is optimal for plenoptic surface reconstruction.

5.2. Assessment of LF FSI methodology

To evaluate the performance of the LF FSI methodology using synthetic experiments, a volume of 40×40×24 mm^3 (-12 mm to 12 mm in depth around the focal plane) is randomly seeded with particles, representing flow field information. We use a stationary Gaussian vortex ring analytical equation to displace these particles over time (Fahringer and Thurow, 2018). Behind this flow field, we simulate a flat plate with a speckle pattern (represented by round dots) on its surface to oscillate between depths of 12 mm and 18 mm. Plenoptic images are generated from these particles and speckle pattern positions using the plenoptic synthetic image generation tool (Fahringer et al., 2015). The particles are in the form of 3 × 3 pixels of Gaussian blobs of intensity, while the speckled dots on the flat plate range from 5 to 9 pixels in image space. In this analysis, although the flow and structure motion are not coupled, both types of information are present in the same plenoptic image. The camera configuration and surface reconstruction follows that presented in Table 1, while Table 2 outlines the configuration of the flow field reconstruction used in this analysis.

5.2.1. Assessment of decomposition of particles and surface images

Figure 5.a represents the eigenvalues of the combined particle and surface images arranged from the highest to the lowest values. From this figure, the few high-energy eigenmodes dominate and represent surface information. Similarly, all the other eigenmodes dominantly represent the particle information and are used to extract the particle images.

Table 2
Configuration of synthetic analysis for LF FSI

Particle speckle pattern separation	**Configuration**
Image resolution	6600 × 4400
Number of images	1000
Perspective image size	942 × 628
Number of perspectives	81
Flow field reconstruction	**Configuration**
Volume of interest	x=[-20 to 20] mm, y=[-20 to 20] mm, z=[-12 to 12] mm
MART reconstruction	Number of iterations = 8 Relaxation factor = 0.8 Voxel size = 0.1 mm
Cross-correlation	Window size =[64,48,32,32] Window overlap = [32,24,16,16]

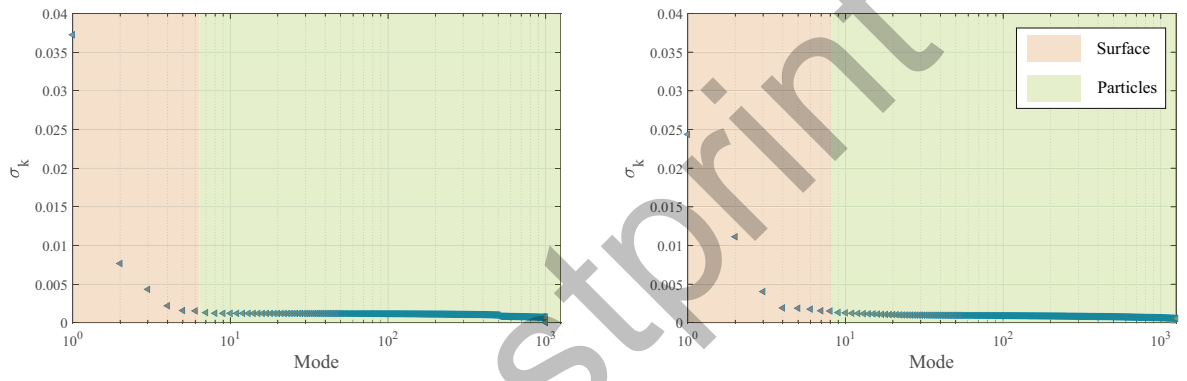

(a) (b)

Figure 5: Eigen values of combined particle and surface image for moving flat plate experiment from (a) synthetic analysis in Section 5.2 (b) experimental analysis in Section 6.2.

The precision of the particle surface separation process is shown by comparing the peak signal-to-noise ratio (PSNR), structural similarity (SSIM), and reconstruction quality (q^*) of the separated particle and surface image. PSNR is defined as the ratio of the peak dynamic range of pixel intensities to the mean squared error (MSE) as given in Equation 4. MSE is the difference between the true image and the reconstructed image.

$$\mathrm{PSNR} = 10\log_{10}\frac{{I_{max}}^2}{\sqrt{\mathrm{MSE}}} \tag{4}$$

$$\mathrm{MSE} = \frac{\sum_i (I_i - \hat{I}_i)^2}{n} \tag{5}$$

Here, I is the image, $\hat{I}$ is the reconstructed image and I_{max} is the maximum possible value of the image intensity. Standard reconstruction quality (q^*) is defined as the normalized correlation coefficient of the intensity of the true

Table 3
Comparison of reconstructed image from POD at different particle densities

	PSNR		Reconstruction quality		SSIM	
PPM	Particle	Background	Particle	Background	Particle	Background
0	Inf	Inf	1	1	1	1
0.029	29.361	15.463	0.985	0.986	0.979	0.881
0.053	28.620	14.545	0.982	0.971	0.977	0.850
0.077	27.798	13.868	0.976	0.966	0.976	0.838
0.101	27.527	13.053	0.968	0.940	0.972	0.828
0.124	26.928	12.417	0.962	0.936	0.965	0.820

image I and the intensity of the reconstructed image $\hat{I}$ as given in Equation 6.

$$q^* = \frac{\sum_i I_i \hat{I}_i}{\sqrt{\sum_i I_i^2 \sum_i \hat{I}_i^{\,2}}} \tag{6}$$

The structural similarity index considers a similarity of luminance, structure, and contrast between a reconstructed image and a true image. It is defined in Equation 7.

$$\text{SSIM} = \frac{(2\mu_I \mu_{\hat{I}} + C_1)(2\sigma_{I\hat{I}} + C_2)}{(\mu_{\hat{I}}^2 + \mu_I^2 + C_1)(\sigma_I^2 + \sigma_{\hat{I}}^2 + C_2)} \tag{7}$$

In this equation, μ_I and $\mu_{\hat{I}}$ is the mean, and σ_I and $\sigma_{\hat{I}}$ is the variance of the true and reconstructed images, respectively. $\sigma_{I\hat{I}}$ is the covariance value and C_1 and C_2 are the constants as defined in Wang et al. (2004).

Table 3 shows the comparison of the reconstructed image quality of particles and background images in terms of PSNR, standard reconstruction quality, and SSIM for images with a different number of particles per microlens (ppm). The reconstruction quality and SSIM for individual images without particles or background are 1 as it is the maximum possible value for both these variables. As the particle density increases, we observe that the reconstruction quality, SSIM, and PSNR decrease slightly. This is a result of blending particle and surface information, compromising the distinct separation of information in the form of POD modes. Furthermore, as the separated images derived from POD modes serve as approximations of only pure surface or particle information, there is a small loss in image sharpness. However, both reconstruction quality and SSIM are still greater than 0.9 for all particle images and greater than 0.8 for all surface images. This suggests that the separated particle and structure images are close to the individual particle and structure images.

5.2.2. Assessment of structural motion and flow field reconstruction

The separated images are used to reconstruct the 3D flow field and structure. Table 2 shows the detailed configuration for the surface and flow field reconstruction. We compare the flow field solutions obtained from the separated particle images (flow with structure) and from images of particles without structure (flow without structure) to the ideal solution, using images with a particle concentration of 0.054 ppm. The ideal solution is obtained by cross-correlating volumes filled with 3×3 Gaussian particles whose positions are defined based on the Gaussian vortex ring equation. This solution carries with it the limitations of using cross-correlation to determine particle displacement but removes any artifacts associated with the tomographic reconstruction process. Figures 6.a, 6.b and 6.c present isocontours of the reconstructed vorticity magnitude. In all cases, the vorticity isocontours reveal a distinct vortex structure. However, Figures 6.b and 6.c show multiple small blobs of vorticity scattered throughout the volume. These structures arise from measurement noise, which is dominated by higher uncertainty in the depth-wise velocity component due to small angular information. These structures are more prevalent in the reconstruction acquired from flow with structure images compared to that acquired from flow without structure images. This indicates that the decomposition process does have a minor effect on the data quality. The contour surrounding the vortex ring is also less distinct in the flow with structure solution. The combined effect of smoothing of the particle intensities, the addition of

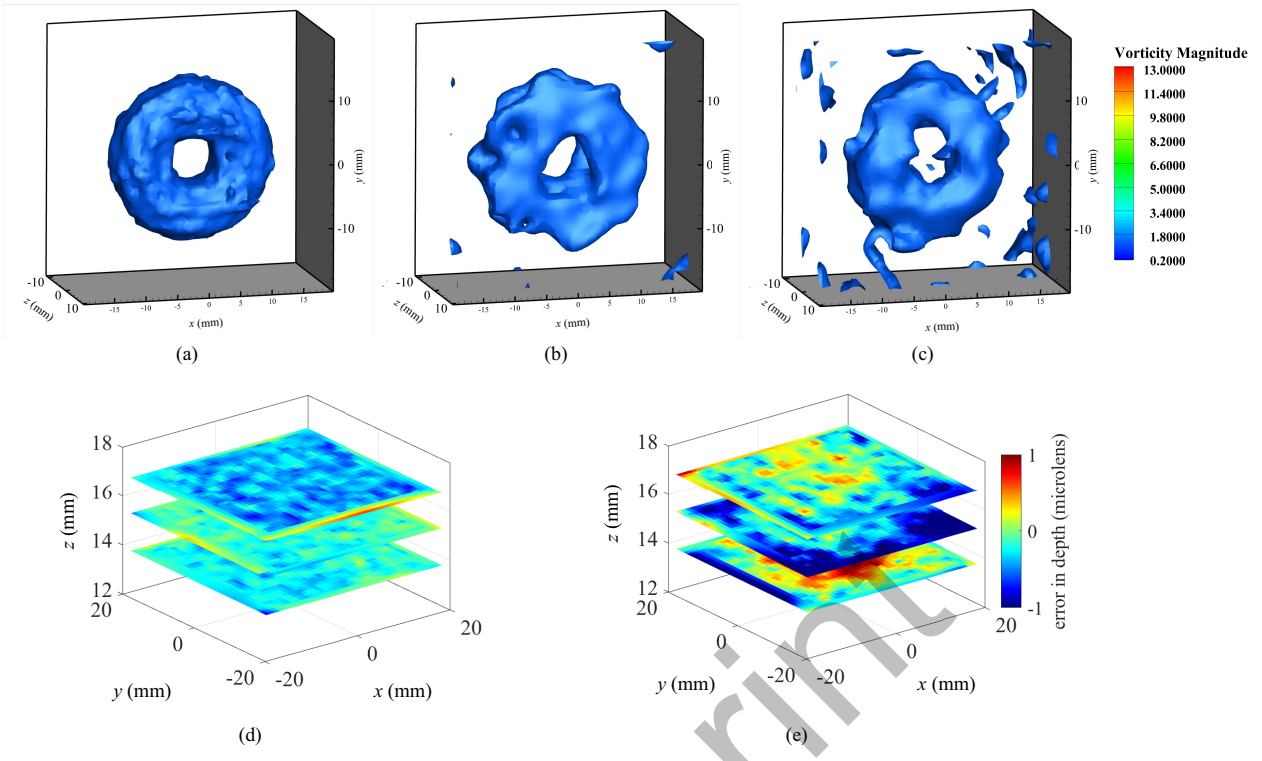

Figure 6: Isosurfaces of vorticity magnitude for (a) ideal solution (b) flow without structure, (c) flow with structure. Surface reconstruction at different depths with speckle images from (d) structure without flow (e) structure with flow.

noise from the surface, and the loss of some particles during the separation process results in this degradation. Despite these imperfections, the dominant flow feature is observable and the vorticity contour range is similar in all cases. Thus, the solution acquired from the flow with structure is comparable to the solution acquired from flow without structure.

Figures 6.d and 6.e show the reconstructed surface at different planes as it moves between 12 and 18 mm behind the vortex ring. Figure 6.d shows the surface reconstructed from the images of the speckle pattern without the presence of any particles (structure without flow). Figure 6.e shows the reconstructed surface from images with the speckle pattern separated from the combined particle-surface images (structure with flow). The color map on each surface shows the corresponding error in depth estimation associated with the surface plot at that location. The color map shows a higher error in surface reconstruction for a structure with flow compared to a structure without flow. Thus, the presence of particle information affects surface reconstruction even after particle-surface separation.

Figure 7 illustrates the standard deviation of the measurement of both the flow field and the surface. The standard deviation of flow measurement is presented in a bar chart, breaking down the uncertainty in each velocity component (u, v, and w) separately. The w error is considerably larger in both cases compared to the in-plane velocities (u and v), primarily due to the low angular baseline of the plenoptic camera. The graph reveals an increase in uncertainty in all components u, v, and w when the surface is introduced into the particle image. The increase in uncertainty of the w component is comparatively larger than the increase in plane velocities. However, there is less than 16% (less than 0.3 microlenses) increase in uncertainty for flow with structure as compared to the absence of structure.

Similarly, the uncertainty in the surface measurement is quantified with varying particle density, as shown in the bar chart in Figure 7.b. The chart indicates that an increase in the number of particles correlates with an increase in the standard deviation of surface measurement. While the standard deviation in surface reconstruction increases several (2 to 3) times with the introduction of particles, it remains around 0.5 microlenses even for higher particle density.

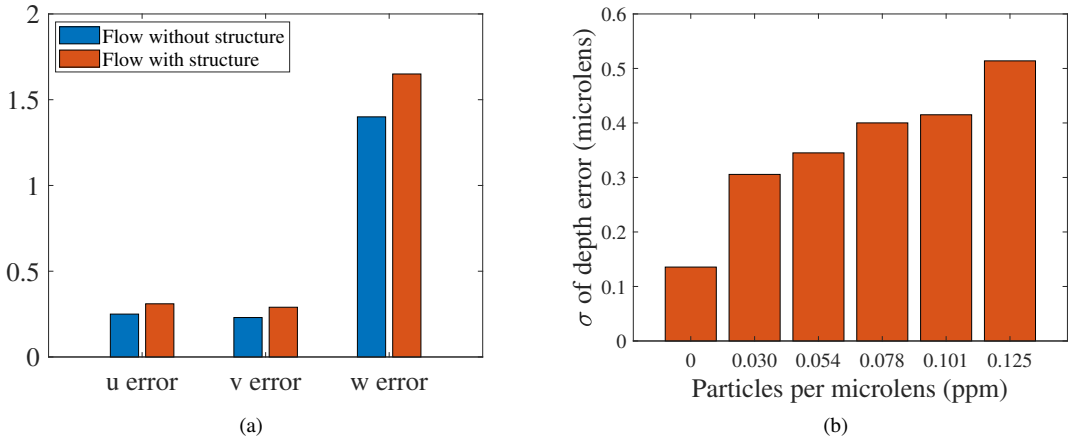

Figure 7: (a) Standard deviation in velocity measurement with LF FSI methodology. (b) Standard deviation of reconstructed surface point cloud with LF FSI methodology.

6. Evaluation of LF FSI methodology using experimental data

In this section, we validate the LF FSI methodology using experimental analysis. Plenoptic particle image velocimetry for flow field measurement is a well-established technique that has undergone rigorous testing and verification across various flow field scenarios (Fahringer et al., 2015; Chen and Sick, 2017; Jones et al., 2018; Raghav et al., 2019; Gururaj et al., 2021). Additionally, the use of POD for processing PIV images is well-established, as demonstrated in Mendez et al. (2017); Baghaie (2019). While the validation of flow field information from a plenoptic camera and the use of POD-based methods in PIV are well documented in the literature, the surface reconstruction aspect of simultaneous flow and structure reconstruction has not been validated. Therefore, this section focuses on the latter.

6.1. Assessment of surface reconstruction

For the verification of the surface reconstruction technique, a simple benchtop experimental set-up with a plenoptic camera and a surface to be tracked along a computer-controlled translation stage is arranged, as shown in Figure 8. The flat surface features an affixed speckle pattern that is used to track the displacement of the plate. The plate is displaced every 3 mm along the depth between -15 and 15 mm from the focal plane. A Thorlabs 300mm linear motorized translation stage with an accuracy of ± 5 μm is used to move an attached flat surface. An Imperx B6620 CCD camera with a hexagonal microlens array in front of the sensor is used for imaging with a 60 mm focal length main lens at a magnification of -0.6.

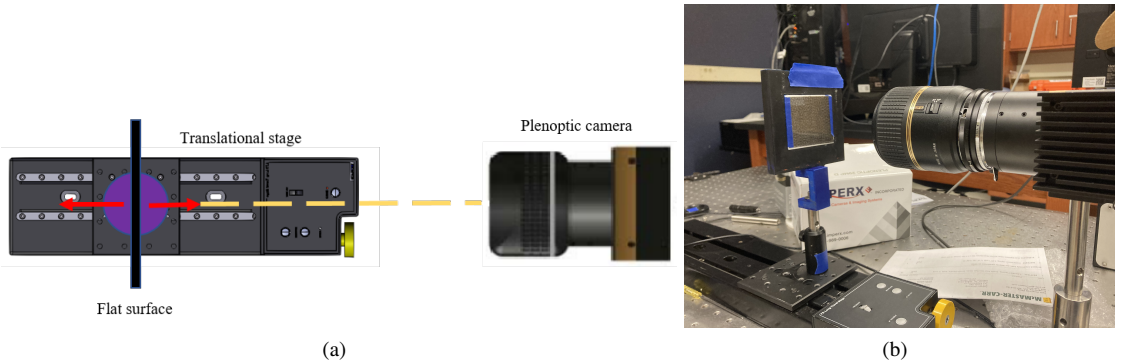

Figure 8: (a) Schematic of experimental setup (b) bench-top experimental setup for assessment of surface reconstruction.

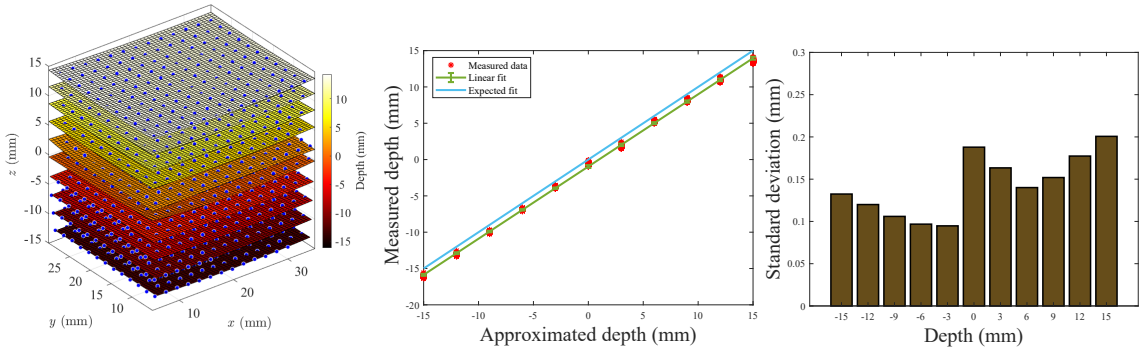

Figure 9: (a) Reconstructed plate position at different depth locations. (b) Approximated and measured depth positions of the plate. (c) Standard deviation of measured depth positions.

Figure 9.a shows the reconstructed surface at different depths, where blue dots represent the reconstructed point cloud fitted with a surface. Figure 9.b plots the measured vs. expected depth of the flat surface at various positions. A reference line with a slope of 1 represents the expected linear fit for a flat plate perpendicular to the camera. The fitted slope using the disparity bundling method is 0.99, with a small offset likely due to the thickness of the calibration plate. This indicates that the reconstructed plate position closely matches the expected fit with minimal error. Figure 9.c presents the standard deviation of the reconstructed plate position at different depths around the best-fit plane. Due to varying angular information in plenoptic images, the standard deviation changes with depth. It is highest at the focal plane, decreases on both sides and rises again as depth information blurs further from the focal plane. The average standard deviation across all positions is 0.12 mm, suggesting that the disparity bundling method estimates depth within sub-millimeter uncertainty.

6.2. Assessment of structural motion in presence of PIV particles

This section assesses the performance of LF FSI in tracking structural motion within a nominally uniform flow seeded with PIV particles, using a single plenoptic camera. Figure 10 shows a schematic of the experimental setup along with a photo of the experiment. The setup specifications are tabulated in Table 4. The experimental arrangement includes a flat plate attached to a translation stage and placed in a water tunnel with a uniform flow of 0.12 m/s. The tunnel is a small open channel with a test section of 6 × 6 inches. A 300 mm motorized translation stage moves the attached flat surface in a trapezoidal motion, reaching a peak velocity of 10 mm/s and peak acceleration of 35 mm/s^2, oscillating back and forth. The plate is shifted between 5 and 17 mm from the focal plane (z = 0 mm) to ensure that the structure does not pass through the focal plane and that there are enough particles in front of the surface for analysis. The speckle pattern is printed on waterproof paper and affixed to a flat structure, which is connected to the motorized translation stage.

Images are captured with a high-speed plenoptic camera, as described in (Thurow et al., 2021). The camera features a Phantom VEO4K CMOS sensor (4096 × 2304 pixels, 0.0067 mm pixel size) and a hexagonal microlens array (248 × 151 resolution, 0.077 mm pitch, 0.308 mm focal length). The main lens has a 60 mm focal length, and the object is imaged at a magnification of -0.50 through a 70-50 mm relay lens setup. The volume is illuminated by a 527 nm Nd:YLF Photonics dual-head laser, with 55 µm polyamide particles at densities up to 0.065 ppm. 12-bit images are captured at the rate of 200 frames per second (fps). Synchronization of the camera, stage, and laser is achieved using LabVIEW and a National Instruments data acquisition system. Calibration is performed using Direct Light Field Calibration (DLFC) (Hall et al., 2018), generating 4$^{\text{th}}$ order polynomial coefficients to relate image and world space.

Figure 11.a shows the center perspective view extracted from the plenoptic image. 10 cycles of periodic motion of surface forming a collection of 1250 time-resolved perspective images are acquired. Figure 5.b illustrates the eigenvalues associated with the POD modes. High-energy POD modes are used to reconstruct the moving surface, while the remaining modes are used to reconstruct particle images, as shown in Figures 11.b and 11.c, respectively.

The 3D point cloud and the fitted surface reconstructed using speckle pattern images are presented in Figure 12.a. The figure showcases a smooth 3D surface that closely aligns with the expected plate position between 5 and 17 mm. The small curvature of the measured plate profile is from fitting the generated point cloud with some uncertainty that

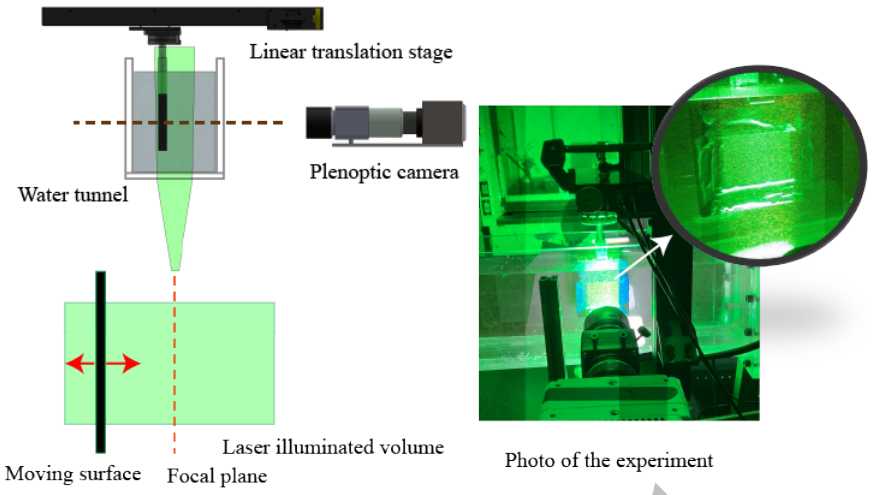

Figure 10: Schematic of the experimental setup of a moving flat plate.

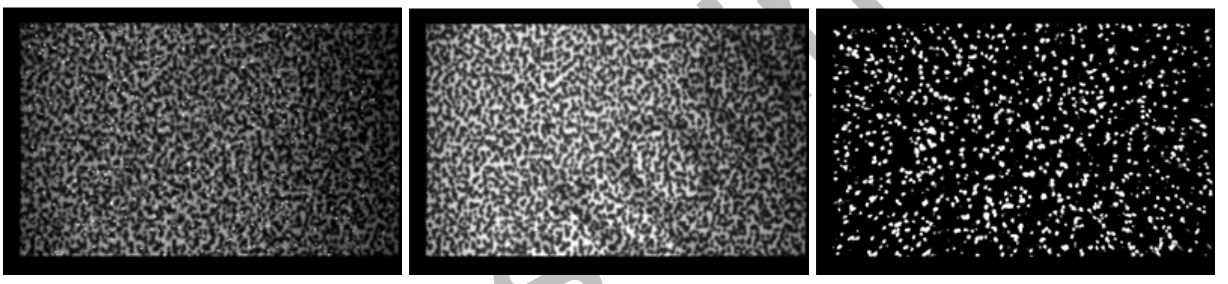

(a) (b) (c)

Figure 11: (a) Simultaneous particle and surface image (b) separated surface image (c) separated particle image.

is exacerbated by the camera vignetting (Thurow et al., 2020). Since the velocity profile is trapezoidal which includes acceleration, uniform velocity, and deceleration phases, the first two and the last two surfaces appear closer, while the middle surfaces are at equal intervals. The velocity of the surface is calculated using a central difference scheme from the reconstructed surface points. The mean velocity profile of the surface for experiments with different particle concentrations is plotted in Figure 12.b. It is compared with the case where there are no particles (represented by the green line) and the prescribed profile (represented by the sky blue line). We observe that the acceleration, constant velocity, and deceleration phases in the trapezoidal profile are distinct for all particle densities. These profiles align closely to the prescribed profile, and the standard deviation of the obtained velocity is within 11% of the mean velocity at any instance. These results suggest that the LF FSI method is robust against experimental challenges, such as light scattering and image noise, and effectively captures structural information across different particle densities.

6.3. Application to a fluttering flexible membrane

In this section, we use a single plenoptic camera and a stereo camera pair to simultaneously observe the fluttering of a flexible membrane in a water tunnel. Figure 13 shows the experimental setup. The flexible membrane under observation is a conventional flag fabricated from silicone with vertically embedded brass rods. The flag, measuring 57.2 mm $\times$ 38.1 mm, has an unrestricted length of 44.5 mm due to the presence of an embedded mounting pole at its front. Light gray-colored dots of silicone are applied to the mold and then covered with black-colored silicone during the molding process to form the speckle pattern for surface reconstruction. The speed of the water tunnel is set to 0.82 m/s. At this speed, we observe the flag to oscillate with a frequency of about 12.5 Hz and an amplitude of around

Table 4
Configuration of experimental assessment of flat plate using LF FSI

Equipment	**Setup**
Camera	Phantom VEO4K CMOS camera Sensor size: 5.5 mm Pixel size: 0.0067 mm Resolution: 4096 × 2304
Micro-lens	Radius: 0.077 mm Focal length: 0.308 mm Resolution: 248 × 151
Main lens	60 mm
Laser	Photonics Nd:YLF 527 nm
Particles	Polyamide 55 μm
Translation stage	Thorlabs 300 mm linear stage
Water tunnel	Test section: 6 × 6 inches Flow speed: 0.12 m/s
Surface structure	3D printed with PLA
Speckle pattern	Radius: 8 pixels
Imaging	**Setup**
Magnification	-0.50
Depth of field	40.125 mm
Frame rate	200 fps
Particle speckle pattern separation	**Configuration**
Number of images	1250 images
Perspective image size	496 × 331 pixels
Number of perspectives	81
Surface reconstruction	**Configuration**
Volume of interest	x=[-3 to 45] mm, y=[-3 to 25] mm, z=[12 to 18] mm
Correlation window size	[64,32,32]
Window overlap	[32,16,16]
RANSAC outlier threshold	1 microlens

Table 5
Configuration of the flexible flag

Parameters	**Configuration**
Flag dimensions	57.2 mm (free length 44.5 mm) × 38.1 mm (width) × 1.2 mm (thickness)
Pole cross-sectional dimensions	10.2 mm × 0.51 mm
Material	Silicone body (Ecoflex 00-10) supported by 32 vertical brass rods of 0.8 mm diameter
Mass ratio of free section (μ)	0.096
Aspect ratio of the free section (AR)	0.86
Dimensionless longitudinal rigidity of free section (β)	2.26e-04
Reynolds number based on free section length (Re)	38,200

2.5 mm. The details of flag construction and the dimensionless parameters that govern the flag flutter (as stated in equation 1) for the experimental configuration are listed in Table 5. The linear elastic modulus of the silicone material is estimated using tensile tests. To estimate β, the stiffening effect of the rigid rods on the flag is assessed using a 2D finite element method (FEM). It is noteworthy that the inclusion of vertical brass rods inhibits transverse bending, thereby making the flag's flexural rigidity anisotropic.

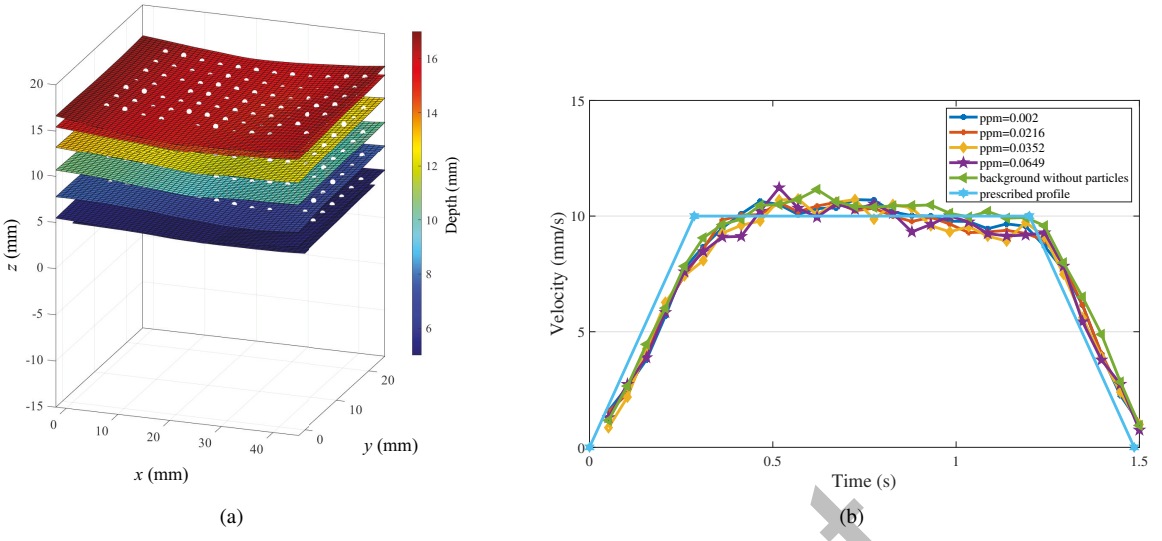

Figure 12: (a) 3D reconstruction of the moving flat plate at different depths in the presence of PIV particles. (b) Velocity profile of the moving surface with its distribution at different depths compared to the prescribed motion profile.

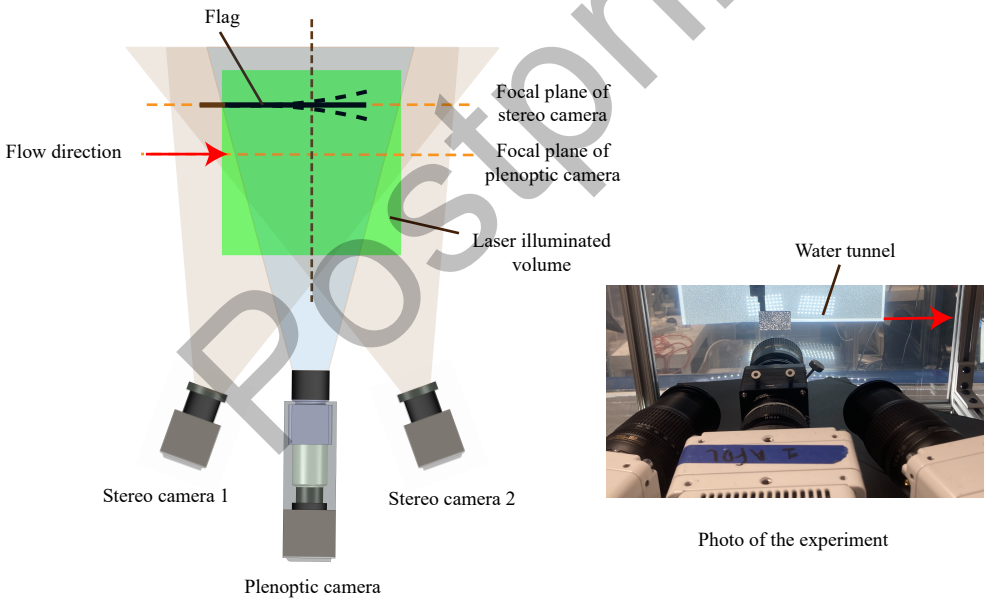

Figure 13: Schematic of the simultaneous plenoptic and stereo camera setup and an actual photo of the experiment.

The detailed configuration of the experimental setup is listed in Table 6. The plenoptic camera configuration is similar to that mentioned in Section 6.2. The stereo camera setup comprises a pair of Phantom VEO 640L cameras placed on either side of the plenoptic camera. The stereo cameras image the flag at a resolution of 1920×1080 pixels with a sensor pixel pitch of 0.01 mm. The focal plane of the stereo cameras corresponds to the plane where the flag is placed, around 11 mm behind the center plane of the laser-illuminated volume. The plenoptic camera is focused on that center plane. The field of view of the plenoptic camera measures around 42 mm $\times$ 15 mm at a magnification of

Table 6
Configuration for flag surface visualization using LF FSI methodology

Imaging	**Setup**
Plenoptic camera magnification	-0.62
Frame rate	1338 Hz
Calibration type	Checkerboard calibration
Plenoptic calibration	Direct light field calibration (polynomial calibration of 3rd order)
Stereo camera calibration	MATLAB stereo camera calibration (pinhole calibration)
Particle speckle pattern separation	**Configuration**
Number of images	3000 images
Perspective image size	512 × 358 pixels
Number of perspectives	81
Surface reconstruction	**Configuration**
Correlation window size	[96, 64, 64]
Window overlap	[32, 16, 16]
RANSAC outlier threshold	1 microlens
Flow fields reconstruction	**Configuration**
MART reconstruction	Number of iterations = 10 Relaxation factor = 0.75 Voxel size = 0.08 mm
Cross-correlation	Window size =[64,48,32,32] Window overlap = [32,24,16,16]
Volume of interest	x=[0 to 42] mm, y=[0 to 15] mm, z=[-15 to 15] mm

around -0.62. In this configuration, most of the flexible portion of the flag is within the field of view, while the rigid stationary base of the flag is not observed, as shown in Figure 13.

A $42 \times 15 \times 32$ mm^3 measurement volume, uniformly seeded with 55 μm polyamide particles at a concentration of approximately 0.062 ppm, is illuminated by an Nd:YLF laser from Photonics Industries. The particle concentration for the experiment is around 0.062 ppm. All three cameras are synchronized using a LabVIEW program with an NI data acquisition system. The volume is calibrated by placing a checkerboard calibration plate at known positions in the volume. Direct Light Field Calibration (Hall et al., 2018) is used to process the plenoptic calibration to generate 3rd order polynomial coefficients. The stereo camera calibration is performed using the MATLAB stereo camera calibration (Zhang et al., 2000). The images are taken at an acquisition rate of 1338 fps. This acquisition rate is selected to keep the particle displacement within 6 to 8 microlenses for optimal PIV processing.

Figure 14 shows the comparison of surface reconstruction of the flag from plenoptic and stereo camera images. Stereo surface reconstruction is performed with the MATLAB stereo reconstruction algorithm. Stereo surface reconstruction includes the following steps: image rectification, disparity identification, and triangulation (Hirschmuller, 2005; Bradski and Kaehler, 2008). The stereo camera coordinate system is transformed to match the coordinate system of the plenoptic system using simultaneously captured calibration images. This is necessary since different calibration methods are used in their respective reconstruction process. Figure 14.a shows the reconstructed 3D surface with both stereo and plenoptic images plotted for three time instances. We observe that the plenoptic camera captures the large-scale deflection much like the stereo cameras. To further assess the surface reconstruction, we plot the two-dimensional envelope traced by the flag with plenoptic and stereo reconstruction as shown in Figure 14.b. Both axes in the plot are normalized by the free length (L) of the flag. The area of the stereo envelope is larger compared to that of the plenoptic envelope; however, the difference between them is relatively small and falls within the uncertainty of plenoptic reconstruction. The tip of the plenoptic flag is slightly shorter compared to the stereo flag. This is attributed to the use of the window-based correlation technique, which limits the spatial resolution such that points near the edges result in low-confidence point clouds and are ultimately filtered out as outliers. In Figure 14.c, the time trace of the filament at a location of $x/L = 0.8$ is compared over multiple cycles of flag oscillation. The figure shows that

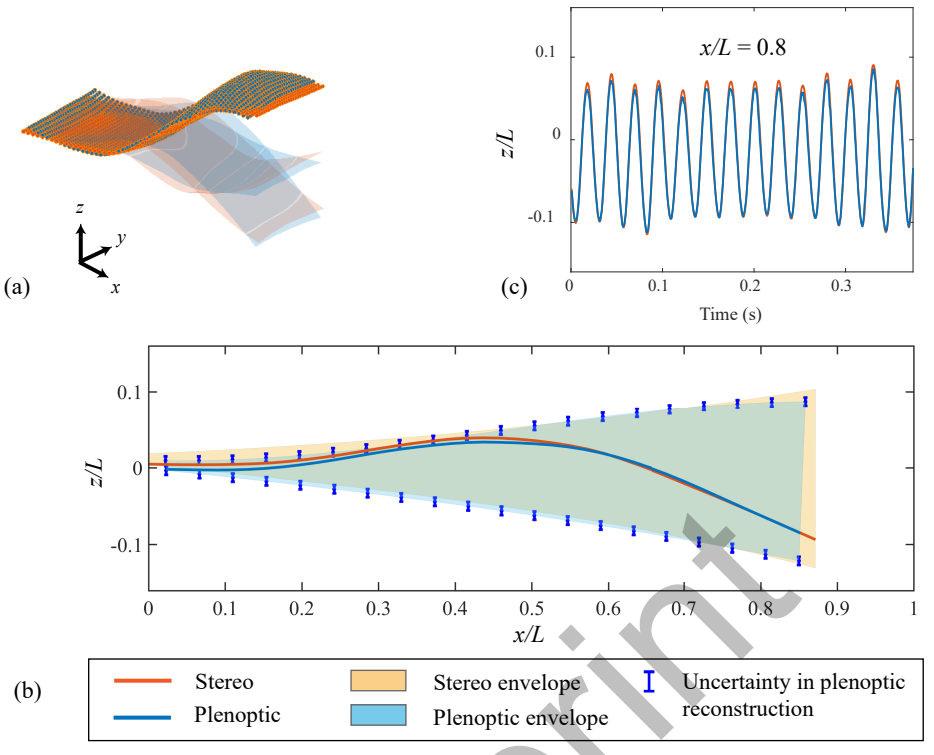

Figure 14: (a) 3D surface reconstruction of a flag at different time instances form simultaneous images taken with stereo (orange) and plenoptic (blue) camera. (b) 2D envelope formed by the flag motion from stereo and plenoptic surface reconstruction. (c) Time trace of the flag filament at $x/L = 0.8$ with stereo and plenoptic reconstruction.

the amplitude of the plenoptic reconstruction is comparable to the stereo reconstruction, the difference being around 2% of the characteristic length of the flag. This is attributed to the fact that plenoptic cameras use a much lower resolution image at a smaller baseline parallax for the reconstruction compared to stereo cameras. In spite of this, the LF FSI methodology captures all the large-scale deflections, and the profile of the time trace of flag tip displacement is comparable to the stereo reconstruction.

Now, we look into the performance of a plenoptic camera to simultaneously capture flow and structure motion. The acquired flow field has been phase averaged and plotted in figures 15 and 16. For phase averaging, we determined the primary oscillating frequency by analyzing the amplitude spectrum of tip displacement, which was found to be 12.5 Hz. Figure 15 shows the three-dimensional view of the flow and structure motion captured for various phases in a flag oscillation cycle (see the Supplementary Material for videos). The color contour on the surface is the maximum principal curvature of the surface plotted at each surface location. We observe both negative and positive curvature on the surface, which changes as the flag oscillates. The figure also shows the isosurface of stream-wise velocity (u) normalized by the free stream flow velocity (U), which clearly shows the contour of lower (blue) and higher (red) velocity regions close to the flag's surface. The behavior of the flow close to the surface changes with the change in the shape of the flag. To further examine the motion of the fluid and the structure in detail, a cross-sectional view of the stream-wise velocity contour at $y = 8$ mm in the same instances as the 3D reconstructed flag position is shown in Figure 16. While the coupled motion of the flag and the flow around it is complex, we observe higher speeds in the vicinity of convex locations as the flag surface bends downwards and lower flow speeds in the vicinity of concave locations as the flag surface bends upwards. This is in line with the continuity equation that flow contraction over the surface should cause the velocity to increase and vice versa. We observe an alternation of this flow behavior along the surface of the flag, whereas opposite effects are expected on the other side of the flag. This phenomenon is expected to correspond to a pressure difference across the flag that governs the flag flutter (Thoma, 1939).

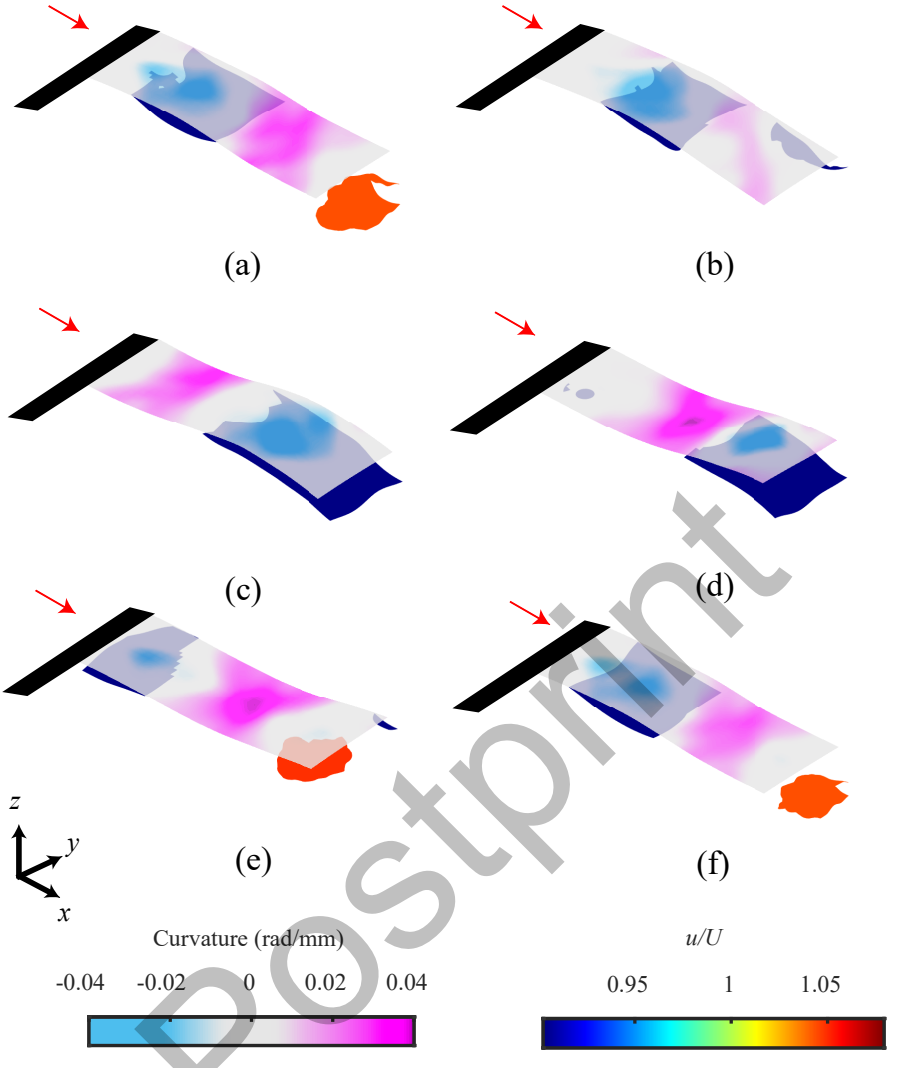

Figure 15: Isosurfaces of normalized stream-wise velocity (u/U) and reconstructed flag with surface curvature at different time instances during a single oscillation period.

Figures 17.a and 17.b show cross-sections of normalized depth-wise velocity with streamlines for the upstroke (flag moving up) and downstroke (flag moving down) conditions. Due to low velocity fluctuations in the FSI regime and the relatively high uncertainty in depth velocity measurements from plenoptic PIV (Fahringer et al., 2015), the w-velocity was estimated using the streamwise gradient of u via the continuity equation ($w = -\int \frac{du}{dx}\, dz$), assuming a 2D incompressible flow ($\frac{dv}{dy} = 0$). This assumption holds in the flag's mid-section, where the v-velocity is negligible. Though we expect future methodological improvements to remove the need for this estimate, the current results still show clear downward flow in the first half and upward flow in the second half of the upstroke, with the opposite trend during downstroke. Figure 17.c shows zoomed-in normalized w-velocity plots with streamlines near the flag surface across three spanwise planes at different flutter phases. The color contours and streamlines show consistent flow behavior along the width of the flag and suggest the absence of strong three-dimensional effects in the measurement volume. Because the flag is in motion, streamlines may intersect the surface depending on its local displacement velocity. If the boundary layer were resolved, we would expect streamlines to align with this velocity vector, roughly normal to the surface. Current measurements don't extend close enough to confirm this. Given the

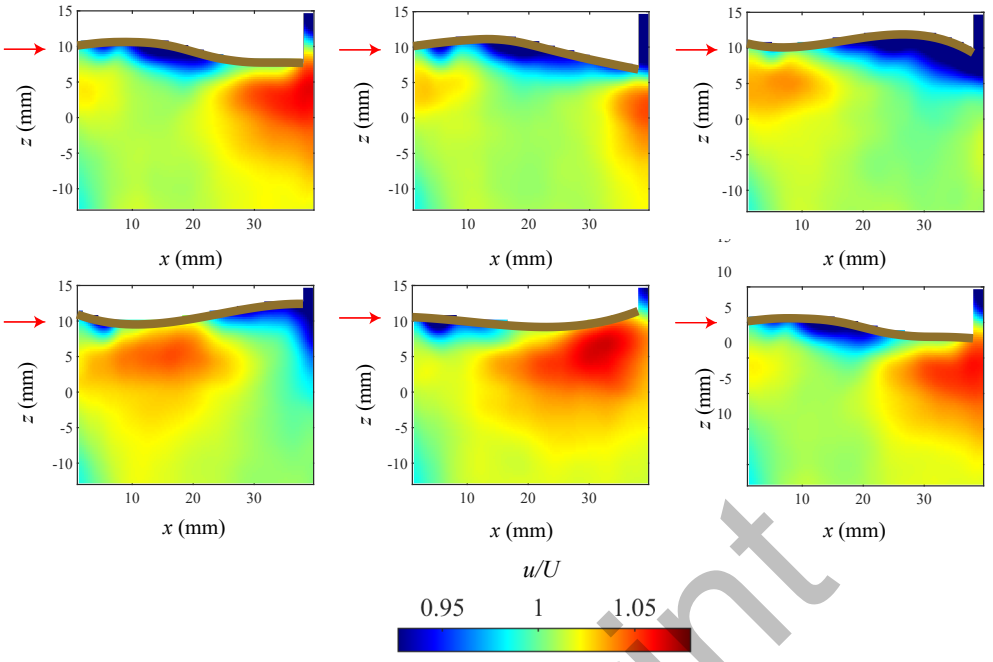

Figure 16: Cross section of normalized stream-wise velocity (u/U) for the same time instances as in Figure 15 at $y = 8$ mm.

resolution, streamlines are expected to intersect at shallow angles when the flag moves up (away from the fluid) and point outward when moving down (into the fluid). Figure 17 broadly reflects this, though the angles are somewhat exaggerated. The main takeaway is that streamlines closely follow the flag's contour along its full length, consistent with a globally attached flow throughout the flutter cycle.

To further validate the 3D plenoptic PIV measurements, a separate 2D PIV experiment was conducted under the same conditions, focusing on the center plane of the flag. Particle images were processed using LaVision DaVis 10.2 with a minimum correlation window size of 32 × 32 pixels. Since the two PIV datasets were not acquired simultaneously and no phase-locking mechanism was available, images were manually selected from different oscillation cycles by visually matching the flag's position and motion phase. The corresponding velocity fields were phase averaged to enable comparison with the plenoptic PIV at equivalent phases. Figure 18 shows the comparison of the 2D and plenoptic results: Figures 18.a and 18.b show normalized streamwise velocity fields from 2D PIV, while Figures 18.e and 18.f present corresponding plenoptic PIV fields along a plane. The size of the final-pass cross-correlation window is indicated by a box near the root of the flag. Qualitatively, large-scale flow features are consistent between both techniques. Elevated streamwise velocities are observed near convex regions due to flow contraction, while velocity is reduced near concave areas where the flow expands. Quantitatively, there is some difference in fluctuation amplitude, with $(U_{\max} - U_{\min})/U_{\text{mean}} = 0.27$ for plenoptic PIV and 0.38 for 2D PIV. This discrepancy is attributed to differences in resolution—about 19 pixels/mm for 2D PIV versus 8 pixels/mm for the plenoptic setup—and a low-pass filtering effect in the plenoptic case due to the larger cross-correlation volume ($\sim 2.6 \times 2.6 \times 2.6$ mm^3) compared to the 2D window ($\sim 1.6 \times 1.6 \times 1$ mm^3, with 1 mm corresponding to the laser sheet thickness). The out-of-plane (w) velocity, estimated from continuity using the plenoptic streamwise velocity, shows spatial patterns similar to the transverse (v) component measured by 2D PIV near the flag surface, as shown in Figure 18. While the major features are consistent across techniques, some mismatches appear near boundaries, suggesting that additional independent measurements may be needed to resolve finer-scale structures. Nonetheless, the overall agreement supports the accuracy of the plenoptic results and the interpretations discussed above. These observations are also consistent with previous flag flow configurations (Gibbs et al., 2014; Jia et al., 2018), strengthening the effectiveness of the LF FSI approach in capturing coupled structure–flow dynamics.

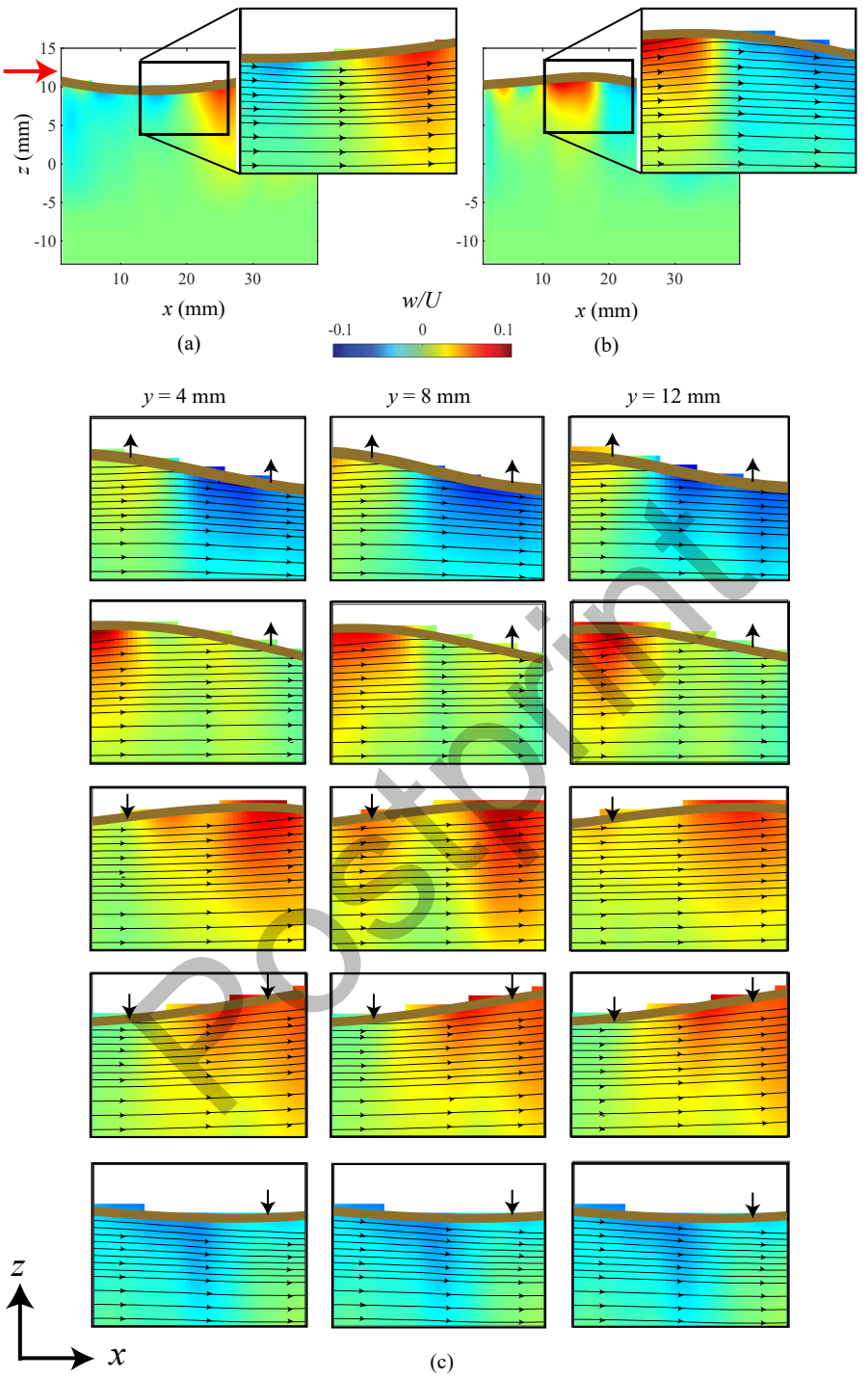

Figure 17: a,b) Normalized w-velocity (w/U) with streamlines at the end of upstroke and downstroke. c) Normalized w-velocity (w/U) for different instances of the flag flutter with streamlines for three different planes at $y = 4$ mm, $y = 8$ mm, and $y = 12$ mm along the flag width. The arrows on the surface indicate the local direction of surface motion, whereas the absence of arrows indicates that the velocity is low or zero.

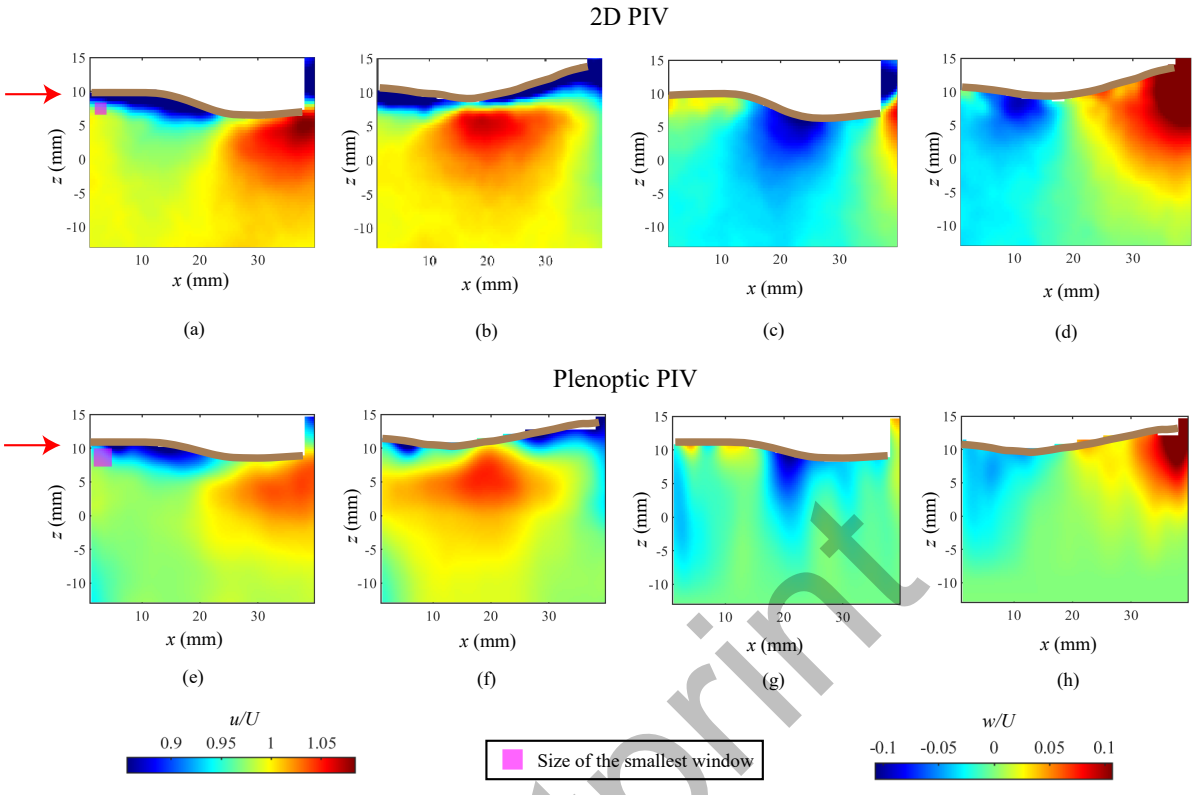

Figure 18: a,b) u/U-velocity (streamwise velocity) contour and c,d) w/U-velocity (transverse velocity) contour at two different phases of flag deflection from 2-D PIV. c,d) u/U-velocity (streamwise velocity) contour and c,d) w/U-velocity (out of plane velocity calculated from continuity equation) contour at a similar phase of flag deflection at plane $y = 8$ mm from 3D plenoptic PIV results.

7. Conclusion

A new methodology for the simultaneous 3D measurement of both structural and fluid motion using a single camera was introduced and based on the unique capabilities of a plenoptic camera. The method uses a POD-based technique to separate structural and particle information recorded on the same image. A correlation-based depth estimation algorithm is presented that effectively uses information from all of the angular perspectives extracted from a plenoptic image to measure the surface profile. Tomographic reconstruction and correlation-based 3D PIV is performed on the separated particle images to determine the velocity of the flow field present in the volume located in front of the surface. Synthetic and experimental analysis was performed to validate the methodology and suggest that, for a small compromise in uncertainty in both the flow field and the structural measurement, it is possible to obtain high-quality fluid-structure interaction measurements using only a single camera.

The LF FSI methodology described here addresses the need for 3D FSI measurement techniques in experiments with limited optical access or where multi-camera experimental arrangements would be otherwise problematic. In addition, the extended depth of field offered by plenoptic imaging allows encoding information about the structure and the surrounding flow field over larger depths than conventional methods. The surface reconstruction obtained from plenoptic image data is robust and able to capture the large-scale deflections of flexible membranes with performance that is comparable to reconstructions obtained with a conventional stereo-imaging experiment. Furthermore, we demonstrate that POD is effective for separating structural and particle information within the same images, enabling the reconstruction of flow and structural motion from a single experiment using a common calibration. This confers a distinct advantage over traditional methodologies that necessitate separate experiments over fluid and structural domains.

While the ability to obtain volumetric velocity field data was clearly established, the limitations associated with plenoptic PIV are also present in the LF FSI methodology. Notably, the resolution along the optical axis is limited by the aperture size of a single lens imaging system, resulting in higher levels of uncertainty along the optical axis of the camera (i.e., the depth direction). This is a well-known limitation of plenoptic camera-based imaging systems, yielding effectively 3D/2C velocity field measurements. Therefore, this methodology is best suited for high-magnification applications — we recommend a magnification of 0.5 or higher. In addition, the uncertainty of surface measurements increases close to the focal plane and with increasing surface angles; thus, an appropriate positioning of the surface with respect to the camera is desired. Since a plenoptic camera sacrifices spatial resolution for angular information, the spatial resolution of LF FSI is comparatively low. This limits the dynamic range of the flow and structural measurements compared to multi-camera methods. Thus, for a given field of view, LF FSI is more suitable for capturing large-scale flow features and structural displacements. A more comprehensive uncertainty quantification of the experimental flow field measurements, facilitated by simultaneous plenoptic PIV and tomographic PIV measurements, was not performed in this study and represents a valuable direction for future work. Nonetheless, LF FSI offers a promising and viable option for simultaneous flow field and structural measurements in scenarios where multi-camera methods are not feasible.

We have identified several areas of potential improvement in the methodology. Recently, time-resolved particle tracking velocimetry (PTV) has been shown to significantly outperform conventional particle image velocimetry (PIV), particularly in estimating depth velocity components in plenoptic velocimetry (Moaven et al., 2024). Therefore, PTV can be used to acquire depth information with higher accuracy. The disparity calculation using other state-of-the-art methods like inverse-compositional Gauss-Newton (ICGN), optical flow algorithms, etc., may offer further improvements in resolution and quality of depth estimation. The uncertainty in surface reconstruction may be further reduced by introducing spatial smoothness constraints during point cloud reconstruction. Recent advances in physics-informed approaches (Raissi et al., 2019; Cai et al., 2021; Zhou and Grauer, 2023) for flow field reconstruction present further opportunities to investigate a similar approach for the FSI diagnostic. This work provides a starting point for an enhanced FSI diagnostic methodology, integrating governing equations as constraints to regularize acquired surface and flow measurements.

Acknowledgements

The authors acknowledge the assistance of members of the Applied Fluid Research Group, the Advanced Flow Diagnostics Laboratory, Dr. Eldon Triggs, and Mr. Andy Weldon in the Department of Aerospace Engineering at Auburn University. The authors also acknowledge the resources provided by the Auburn University Easley Cluster.

Funding

This research was funded by the National Science Foundation (NSF)–CAREER-2145189 to VR.

CRediT authorship contribution statement

Bibek Sapkota: Methodology, Software, Validation, Formal analysis, Investigation, Data Curation, Writing - Original Draft, Writing - Review & Editing, Visualization. **Holger Mettelsiefen:** Methodology, Validation, Investigation, Writing - Original Draft, Writing - Review & Editing. **Vrishank Raghav:** Conceptualization, Resources, Writing - Review & Editing, Supervision, Project administration, Funding acquisition. **Brian S. Thurow:** Conceptualization, Resources, Methodology, Writing - Review & Editing, Supervision, Project administration.

References

Adelson, E.H., Wang, J.Y., 1992. Single lens stereo with a plenoptic camera. IEEE transactions on pattern analysis and machine intelligence 14, 99–106.

Argentina, M., Mahadevan, L., 2005. Fluid-flow-induced flutter of a flag. Proceedings of the National Academy of Sciences 102, 1829–1834.

Baghaie, A., 2019. Robust principal component analysis for background estimation of particle image velocimetry data, in: 2019 IEEE Long Island Systems, Applications and Technology Conference (LISAT), IEEE. pp. 1–6.

Bhargav, V., Francescato, N., Mettelsiefen, H., Usmani, A.Y., Scarsoglio, S., Raghav, V., 2024. Streamwise directional switching of oscillations in a collapsible tube and its effect on the downstream flowfield. Journal of Fluids and Structures .

Bleischwitz, R., De Kat, R., Ganapathisubramani, B., 2017. On the fluid-structure interaction of flexible membrane wings for mavs in and out of ground-effect. Journal of Fluids and Structures 70, 214–234.

Bradski, G., Kaehler, A., 2008. Learning OpenCV: Computer vision with the OpenCV library. " O'Reilly Media, Inc.".

Cai, S., Mao, Z., Wang, Z., Yin, M., Karniadakis, G.E., 2021. Physics-informed neural networks (pinns) for fluid mechanics: A review. Acta Mechanica Sinica 37, 1727–1738.

Chen, H., Sick, V., 2017. Three-dimensional three-component air flow visualization in a steady-state engine flow bench using a plenoptic camera. SAE International Journal of Engines 10, 625–635.

Clifford, C., Tan, Z., Hall, E., Thurow, B., 2019. Particle matching and triangulation using light-field ray bundling, in: 13th International Symposium on Particle Image Velocimetry.

Dou, Z., Rips, A., Jacob, L., Mittal, R., 2020. Experimental characterization of the flow-induced flutter of a suspended elastic membrane. AIAA Journal 58, 445–454.

D'Aguanno, A., Quesada Allerhand, P., Schrijer, F., van Oudheusden, B., 2023. Characterization of shock-induced panel flutter with simultaneous use of dic and piv. Experiments in Fluids 64, 15.

Elsinga, G.E., Scarano, F., Wieneke, B., van Oudheusden, B.W., 2006. Tomographic particle image velocimetry. Experiments in fluids 41, 933–947.

Fahringer, T.W., Lynch, K.P., Thurow, B.S., 2015. Volumetric particle image velocimetry with a single plenoptic camera. Measurement Science and Technology 26, 115201.

Fahringer, T.W., Thurow, B.S., 2018. Plenoptic particle image velocimetry with multiple plenoptic cameras. Measurement Science and Technology 29, 075202.

Gibbs, S., Fichera, S., Zanotti, A., Ricci, S., Dowell, E.H., 2014. Flow field around the flapping flag. Journal of Fluids and Structures 48, 507–513.

Giovannetti, L.M., Banks, J., Turnock, S., Boyd, S., 2017. Uncertainty assessment of coupled digital image correlation and particle image velocimetry for fluid-structure interaction wind tunnel experiments. Journal of Fluids and Structures 68, 125–140.

Griffith, B.E., Patankar, N.A., 2020. Immersed methods for fluid–structure interaction. Annual Review of Fluid Mechanics 52, 421–448.

Gururaj, A., Moaven, M., Tan, Z.P., Thurow, B., Raghav, V., 2021. Rotating three-dimensional velocimetry. Experiments in Fluids 62, 146.

Hall, E.M., Fahringer, T.W., Guildenbecher, D.R., Thurow, B.S., 2018. Volumetric calibration of a plenoptic camera. Applied optics 57, 914–923.

Hirschmuller, H., 2005. Accurate and efficient stereo processing by semi-global matching and mutual information, in: 2005 IEEE Computer Society Conference on Computer Vision and Pattern Recognition (CVPR'05), IEEE. pp. 807–814.

Hou, G., Wang, J., Layton, A., 2012. Numerical methods for fluid-structure interaction—a review. Communications in Computational Physics 12, 337–377.

Jia, Y., Jia, L., Su, Z., Yuan, H., 2018. Experimental investigation of flow field around the elastic flag flapping in periodic state. Modern Physics Letters B 32, 1840031.

Jones, C., Clifford, C., Thurow, B.S., Mears, L., Arora, N., Alvi, F.S., 2018. Two camera plenoptic piv applied to shock wave-boundary layer interactions, in: 2018 Fluid Dynamics Conference, p. 3705.

Kalmbach, A., Breuer, M., 2013. Experimental piv/v3v measurements of vortex-induced fluid–structure interaction in turbulent flow—a new benchmark fsi-pfs-2a. Journal of Fluids and Structures 42, 369–387.

Klemkowsky, J.N., Fahringer, T.W., Clifford, C.J., Bathel, B.F., Thurow, B.S., 2017. Plenoptic background oriented schlieren imaging. Measurement Science and Technology 28, 095404.

Liu, H., Zhou, W., Cai, X., Qian, T., Wu, F., 2019. Experimental research on 3d particle tracking velocimetry based on light field imaging. Proceedings of Global Power and Propulsion Society .

Mendez, M., Raiola, M., Masullo, A., Discetti, S., Ianiro, A., Theunissen, R., Buchlin, J.M., 2017. Pod-based background removal for particle image velocimetry. Experimental Thermal and Fluid Science 80, 181–192.

Mitrotta, F.M., Sodja, J., Sciacchitano, A., 2022. On the combined flow and structural measurements via robotic volumetric ptv. Measurement Science and Technology 33, 045201.

Moaven, M., Gururaj, A., Raghav, V., Thurow, B., 2024. Improving depth uncertainty in plenoptic camera-based velocimetry. Experiments in Fluids 65, 49.

Moré, J.J., 2006. The levenberg-marquardt algorithm: implementation and theory, in: Numerical analysis: proceedings of the biennial Conference held at Dundee, June 28–July 1, 1977, Springer. pp. 105–116.

Ng, R., Levoy, M., Brédif, M., Duval, G., Horowitz, M., Hanrahan, P., 2005. Light field photography with a hand-held plenoptic camera. Ph.D. thesis. Stanford university.

Nila, A., Phillips, N., Bomphrey, R., Bleischwitz, R., de Kat, R., Ganapathisubramani, B., 2016. Optical measurements of fluid-structure interactions for the description of nature-inspired wing dynamics, in: 2016 RAeS Applied Aerodynamics Conference.

Raghav, V., Clifford, C., Midha, P., Okafor, I., Thurow, B., Yoganathan, A., 2019. Three-dimensional extent of flow stagnation in transcatheter heart valves. Journal of the Royal Society Interface 16, 20190063.

Raissi, M., Perdikaris, P., Karniadakis, G.E., 2019. Physics-informed neural networks: A deep learning framework for solving forward and inverse problems involving nonlinear partial differential equations. Journal of Computational physics 378, 686–707.

Roberts, W.A., Thurow, B.S., 2017. Correlation-based depth estimation with a plenoptic camera. AIAA Journal 55, 435–445.

Safi, H., Phillips, N., Ventikos, Y., Bomphrey, R., 2017. Implementing fluid-structure interaction computational and empirical techniques to assess hemodynamics of abdominal aortic aneurysms. Artery Research 20, 55–56.

Saiz, G.G., Sciacchitano, A., Scarano, F., 2022. On the closure of collar's triangle by optical diagnostics. Experiments in Fluids 63, 128.

Scarano, F., Riethmuller, M.L., 2000. Advances in iterative multigrid piv image processing. Experiments in fluids 29, S051–S060.

Shelley, M.J., Zhang, J., 2011. Flapping and bending bodies interacting with fluid flows. Annual Review of Fluid Mechanics 43, 449–465.

Sigrist, J., 2015. Fluid-Structure Interaction: An Introduction to Finite Element Coupling. Wiley. URL: https://books.google.com/books?id=j_w1CgAAQBAJ.

Skupsch, C., Brücker, C., 2013. Multiple-plane particle image velocimetry using a light-field camera. Optics Express 21, 1726–1740.

Song, Y., Qian, Y., Zhang, T., Yin, J., Wang, D., 2022. Simultaneous measurements of bubble deformation and breakup with surrounding liquid-phase flow. Experiments in Fluids 63, 83.

Sotiropoulos, F., Borazjani, I., 2009. A review of state-of-the-art numerical methods for simulating flow through mechanical heart valves. Medical & biological engineering & computing 47, 245–256.

Thoma, D., 1939. Warum flattert die fahne. Mitteilungen des Hydraulischen Instituts der Technischen Hochschule Muechen 9, 30–34.

Thurow, B.S., et al., 2020. Depth-of-field reduction due to blurring in a relayed plenoptic camera and mitigation via deconvolution. Measurement Science and Technology 31, 055403.

Thurow, B.S., et al., 2021. Perspective on the development and application of light-field cameras in flow diagnostics. Measurement Science and Technology 32, 101001.

Vogel, S., 1989. Drag and reconfiguration of broad leaves in high winds. Journal of Experimental Botany 40, 941–948.

Wang, Z., Bovik, A.C., Sheikh, H.R., Simoncelli, E.P., 2004. Image quality assessment: from error visibility to structural similarity. IEEE transactions on image processing 13, 600–612.

Watanabe, Y., Suzuki, S., Sugihara, M., Sueoka, Y., 2002. An experimental study of paper flutter. Journal of fluids and Structures 16, 529–542.

Zhang, J., Childress, S., Libchaber, A., Shelley, M., 2000. Flexible filaments in a flowing soap film as a model for one-dimensional flags in a two-dimensional wind. Nature 408, 835–839.

Zhang, P., Carretto, A., Porfiri, M., 2020. Simultaneous digital image correlation/particle image velocimetry to unfold fluid–structure interaction during air-backed impact. Journal of Fluids and Structures 95, 102980.

Zhang, P., Porfiri, M., 2019. A combined digital image correlation/particle image velocimetry study of water-backed impact. Composite Structures 224, 111010.

Zhou, K., Grauer, S.J., 2023. Flow reconstruction and particle characterization from inertial lagrangian tracks. arXiv preprint arXiv:2311.09076 .